Accepted Manuscript

Combined Airborne Profiling over Fram Strait Sea Ice: Fractional Sea-Ice Types, Albedo and Thickness Measurements

C.A. Pedersen, R. Hall, S. Gerland, A.H. Sivertsen, T. Svenøe, C. Haas

PII: S0165-232X(08)00133-X
DOI: doi: 10.1016/j.coldregions.2008.08.004
Reference: COLTEC 1330

To appear in: *Cold Regions Science and Technology*

Received date: 31 October 2007
Accepted date: 16 August 2008

Combined Airborne Profiling over Fram Strait Sea Ice: Fractional Sea-Ice Types, Albedo and Thickness Measurements

C. A. Pedersen [a,*] R. Hall [a,1] S. Gerland [a] A. H. Sivertsen [b] T. Svenøe [a] C. Haas [c,2]

[a] *Norwegian Polar Institute, Tromsø, Norway*

[b] *Fiskeriforskning, Tromsø, Norway*

[c] *Alfred Wegner Institute for Polar and Marine Research, Bremerhaven, Germany*

Abstract

This paper presents the data collected during an expedition from the marginal ice zone into the multi year sea ice in the Fram Strait in May-June 2005 to measure the variance in sea-ice types, albedo and thickness. It also describes the techniques used to analyze the data. The principal information from the methodologies applied derives the sea-ice types from digital photography, the spectral and broadband reflectance from spectrometer measurements and the total sea-ice thickness profile from an electromagnetic-probe. A combination of methods was used to extract more information from each data set compared to what traditionally are obtained. The digital images were standardized, textural features extracted and a trained neural network was used for classification, while the optical measurements were normalized and standardized to minimize effects from the set up and atmospheric conditions. Measurements from June 3rd (before the onset of summer melt) showed that the fractional sea-ice types had large spatial variability, with average fractions for snow-covered sea ice of 81.0%, thick bare ice 4.0%, thin ice 5.3% and open water 9.6%, hence an average ice concentration of 90.3%. The average broadband reflectance factor was 0.73, while the average total sea-ice thickness (including snow) was 2.1 m. Relative high correlations were found between the measured albedo and sea-ice concentration (0.69). The paper also addresses the lessons learned for future fusion of data from large field campaigns.

Key words: sea ice, airborne measurements, albedo, classification

* Corresponding author.
Email address: christina.pedersen@npolar.no (C. A. Pedersen).
[1] Present address: Kongsberg Satellite Services, Tromsø, Norway
[2] Present address: University of Alberta, Edmonton, Alberta, Canada

1 Introduction

Scientific-based operations in the polar regions are limited, mainly due to the cost, ship and helicopter availability and competition from other scientific programs. Therefore, when opportunities to collect multiple data sets arise, it is important to co-ordinate all activities to ensure that not only are as many parameters as possible studied efficiently, but also that the data can be easily combined and compared for further analysis.

This paper describes the data collected during an expedition from the marginal ice zone into the multi-year sea ice in the Fram Strait in May-June 2005 to measure the variance in sea-ice types, albedo and thickness, and the techniques used to analyze the data. Digital images, optical reflectance measurements and electromagnetic thickness measurements were combined to obtain a detailed description of the sea ice physical and optical properties. The classification of sea-ice types involved surfaces identified during winter and early spring conditions, and therefore melt ponds were not included as they did not cover a notably area fraction of the surface at the time of the measurements. A main question addressed is how albedo varies in relation to the type of sea ice. While there is a simple relationship where thick ice has a high albedo and thin ice has a low albedo, this only applies to thin ice covers up to 30 cm thick under cold winter conditions (Laine, 2004). However, under summer conditions in the Arctic Ocean, the correlation between albedo and sea-ice concentration (extent) extracted from remote sensing data are found to be only 0.34 (0.40), with large variability between different areas (Laine, 2004).

Previous studies on classifying sea-ice types from helicopter images have mostly concentrating identifying melt ponds. As part of the Surface Heat Budget of the Arctic Ocean (SHEBA) field experiment aerial photography and video camera flights were completed between spring and autumn in 1998 (Perovich et al., 2002; Tschudi et al., 2001). Perovich et al. (2002) calculated fractions of ice, new ice, ponds and leads using imaging processing software and manually selected thresholds based on the image intensity histograms, while Tschudi et al. (2001) identified melt pond and open water fractions from video images using spectral information in the three color RGB (red-green-blue) bands of the converted images. Derksen et al. (1997) employed low level aerial infrared images for identifying melt pond fractions, and Fetterer and Untersteiner (1998) utilized maximum likelihood algorithms to select a threshold image-intensity to separate pond distribution from ice distribution. More advanced classification tools for detecting sea-ice types have been employed in studies analyzing Synthetic Aperture Radar (SAR) images. Although SAR images have a coarser spatial resolution than the aerial photography presented in this paper, some of the techniques applied can be adapted to digital photography. Bogdanov et al. (2005) used a neural network and linear discriminate analysis together with data fusion to automatically classify SAR sea ice images. They found that substantial improvements were gained by fusion of several data types. Texture statistics from grey level co-occurence matrices was used in Barber and Le Drew (1991). Also several approaches were applied to optical remote sensing data. A data fusion algorithm involved iterative segmentation procedure on SAR images and extraction of spectral characteristics from AVHRR images, resulted in distinguishing between six sea-ice types (Lythe et al., 1999), while Markus et al. (2002) used a threshold based algorithm on individual Landsat bands to distinguish between white ice, bare/wet ice, melt ponds and open water.

2 Observations

The Fram Strait is the main passage of sea ice and water from the central Arctic Ocean to the global ocean. The volume of ice and water passing through the Fram Strait has a significant impact on the global ocean circulation and convection (Kwok et al., 2004; Vinje, 2001). In May-June 2005, the Norwegian Polar Institute led a ship-based field campaign in the Fram Strait (Fig. 1a), in which three sets of airborne measurements were collected by helicopter (Table 1). As the helicopter was ship-based, it was possible to verify the surface conditions pre- and post-flights. The optical measurements required a clear field of view underneath the helicopter, so two separate flights were required to obtain the three components of the dataset. The first flight included digital photography (Canon EOS 350D digital camera) and optical measurements (ADS FieldSpec Pro spectrometer operated with 8° fore-optics), while the second was for electromagnetic (EM) ice thickness measurements. For the optical flight, the digital camera and the fore-optics of the spectrometer were mounted on an aluminum plate and fastened to the floor of the helicopter looking down (Fig. 2).

[Fig. 1 about here.]

[Table 1 about here.]

[Fig. 2 about here.]

The position, speed and altitude of the helicopter were logged with a Global Positioning System (GPS) receiver, and the altitude and speed of the helicopter were restricted so as to obtain over-lapping images at a sampling frequency of 5 s. A typical optical flight had an image footprint of 200 m in flight direction and 150 m across flight direction with 50-75 m overlap between successive images. In reality, each pixel in the image footprint was rectangular due to the speed of the helicopter and the exposure time of the camera.

A typical footprint for the spectrometer was for simplicity assumed to be a circle with a diameter of 15-25 m, but as with the pixels, the spectrometer footprint was an ellipse due to the helicopter movement during the time taken to conduct a measurement. The reflectance measurements and digital images were co-located post-flight based on GPS time and position.

EM ice thickness measurements were performed continuously along the helicopter flight track with a towed sensor (EM bird). This is a 3.4 m long, 105 kg light cylindric instrument operated at an elevation of 15 to 20 m above the ice surface and suspended with a 20 m long tow cable. It was operated with a signal frequency of 3.68 kHz (Haas et al., 2008). With the EM system, the height of the bird above the ice/water-interface was determined from the strength of the inphase component of the received secondary EM field (Haas et al., 2008). Ice-plus-snow thickness, or total thickness, was obtained by subtracting the birds elevation above the snow/air-interface measured with a laser altimeter which was also integrated in the bird. Hereafter "total thickness" is referred to as "ice thickness". With a sampling frequency of 10 Hz and typical flight speeds of 60 to 80 knots the distance between individual measurement points on the ice is about 3 to 4 m. The accuracy of the EM measurements is +/- 0.1 m over level ice. As shown by Haas et al. (1997) and Pfaffling et al. (2007), the accuracy is not strongly affected by porosity or salinity differences of the ice types discussed in this paper. However, due to the footprint of the EM method of up to 50 m the maximum thickness of pressure ridges can be strongly underestimated. As the EM measurements were collected on a separate flight afterwards, they could not be directly compared to the other measurements due to a slightly different track and a fast drifting ice cover (Fig. 1b).

The spectral albedo is the ratio of reflected to incident irradiance (solar radiation integrated over the hemisphere), while spectral reflectance is the ratio of reflected to incident radiance (solar radiation over a restricted field-of-view). The measurement collected here was the spectral reflectance factor (spectral RF), the ratio of reflected radiance to incident radiation reflected from a perfect, white, diffuse surface (Spectralon, Nicodemus et al., 1977).

The fore-optics of the spectrometer was mounted behind a Lexan window in the helicopter. After the campaign it was realized that the curvature of the Lexan window acted as a collecting lens in the visible, directing the light towards the for-optic. In addition the Lexan window had absorption bands at 350-380 nanometer (nm), about 1700 nm and above 2200 nm (not shown here). Also the reflectance spectra showed an unexpected peak at UV wavelengths (350-380 nm). It is probable that the Lexan window disturbed the measurements, but the net effect is difficult to assess. However, the spectra was normalized to minimize these effects (Sec. 3.2).

2.1 Description of sea-ice types

The distinction and classification between sea-ice types is not a straightforward task. While the WMO Sea-Ice Nomenclature (Secretary of World Meteorological Organization, 1970) is the accepted reference, it does not easily allow for slight variations in ice cover which can be required in detailed scientific studies. As a result, several scientific studies developed sea ice classification schemes based on the WMO, but modified to account for the many variations observed during field campaigns (Steffen, 1986).

In this paper sea-ice classes have been identified based primarily on their surface optical appearance. Three broad and quite general sea-ice types were identified (Table 2, Fig. 3): snow-covered sea ice, bare thick sea ice and open water. We also included a "thin ice" class, mostly consisting of brash ice (a mixture of newly formed thin ice, ice floes and open water), because the small scale variability between ice floes and open water is too fine to be resolved by the classification scheme described (Sec. 3.1.3). The classes correspond well with other ice types chosen for classification (Massom and Comiso, 1994), as the unambiguous distinction of more ice types may be difficult.

Most of the sea ice was covered with optically thick snow (*i.e* snow thickness above 5 cm (Brandt et al., 2005)) at the time of the measurements. However, for some areas the snow had blown away leaving exposed bare ice. Some of the bare ice areas may have been melt ponds or flooded snow/ice at a previous time, but they where refrozen at the time of the measurements. Snow-covered and bare sea ice were separated mainly based on color, as snow has a white appearance compared to the blue-green bare ice.

The thin ice class covers the broadest range of types with a wide range in spectral reflectivity. Optically, it can be thought of as an intermediate type between thick blue-green bare ice and open water. The open water is easily classified with its dark appearance due to the relatively constant 0.07 spectral albedo value over the visual part of the spectrum (Brandt et al., 2005). After the onset of summer melt the situation can be quite different with large areas of melting snow and melt ponds on the ice. However, the techniques described in the next sections are general, and can therefore be expanded to include more sea-ice types.

[Table 2 about here.]

[Fig. 3 about here.]

3 Data analysis

3.1 Digital photography

The images sizes were originally about 2Mb with an average pixel size equivalent to 0.05 m. To reduce processing time the images were down-sampled by averaging over every 10 pixels, giving a down-sampled image of 230x345 pixels and a resolution of approximately 0.50 m.

3.1.1 Image standardization

The exposure time, aperture opening and white balance parameters of the camera were set to automatic, and therefore the color intensity of the images was scaled according to the amount of light and dark pixels in the image. For example, the snow in an image consisting of only snow (bright pixels) seemed darker than the snow in an image consisting of both snow and open water (bright and dark pixels), as also experienced by others (Derksen et al., 1997). The brightness was not constant across the images, and particularly for snow, darker intensities along the edges due to vignetting was observed. However, it did not cause a major problem and was not corrected for. The white balance in the images required corrections, and the images were standardized according to the following iterative procedure (Fig. 4): The first image with good contrast was selected and scaled to an appropriate range. Sub-images of 100 pixels in the flight direction from two overlapping images (last 100 pixels from the first image and first 100 pixels from the second image) were normalized and cross-correlated. The maximum in the cross-correlation matrix gave the position where the two images were aligned or had the best match. The second sub-image was normalized so that the two overlapping sub-images had the same intensity mean and standard deviation. Due to the angle and tilt and variable speed of the helicopter, the images did not completely overlap in the flight direction, and some images required manual adjustments.

[Fig. 4 about here.]

3.1.2 Feature selection

Every pixel in the images was classified separately based on 14 features for texture characterization according to Table 3 (Theodoridis and Koutroumbas, 1999). Features 5-11 were calculated inside a 7×7 pixels sliding window of the grey-leveled indexed image, and provide information related to the grey level distribution of the image, but did not give information about the relative positions of the various gray levels within the image. Features 12-14 are based on the second-order histogram, where pixels are considered in pairs to investigate the relative distance and orientation between them. In Barber and Le Drew (1991), the maximum discrimination between SAR sea-ice types was obtained when considering the grey level co-occurrence matrix with parallel pixels with an interpixel distance of one, and this approach was followed here.

[Table 3 about here.]

The best features for distinguishing between snow-covered ice, thick bare ice, thin ice and open water were selected according to Fisher Discriminant Analysis (Johnson and Wichern, 2002). Fisher Discriminant Analysis is a transformation of the multi-variate observations from the feature space into the Fisher space, where a linear combination of features is selected to achieve maximum separation between the classes. The Fisher discriminant was calculated based on feature vectors with a known classification label, which requires training and test data sets where the classes are known. The training set is used for constructing the classifier, while the test set is used for testing the performance of the classifier. The test and training data sets were created by manual classification of the four sea-ice types. Every combination of features (which results in 16 384 combinations) were tested by calculating the Fisher discriminant, applying the Fisher classification rule (Johnson and Wichern, 2002) and evaluating the total average classification error based on the test set. The set of features giving the smallest classification error was chosen for further investigations.

3.1.3 Classification

A feed-forward back propagation neural network (Haykin, 1999) with 3 layers was used for classification. The first layer has a size (number of neurons) equal to the number of features, the middle (hidden) layer has two times the number of features neurons, and the output layer has one neuron (separating the four classes on the interval [0,1]). All neurons have the log-sigmoid as the activation function. See Haykin (1999) for more information about the neural network options. The neural network was trained by presenting the test set to the network, and the network updated its weight to minimize the sum of squared error to achieve the expected output in an adaptive manner.

Classification based on texture features (calculated over a sliding window) often experiences problems on the edge between classes, *e.g.*, an image consisting of a sharp edge between snow-covered ice and open water will in the classified image often have a small transition zone where intermediate classes (bare ice or thin ice) are detected. Since the median filter is particularly effective in reducing noise, while at the same time preserving edge sharpness (Gonzalez and Woods, 1992), the classified images were median filtered (with a filter size equal to the window size used for extracting the texture features). This approach was also used by others (Tschudi et al., 2001; Derksen et al., 1997). However, it does not completely remove the bias, and we must expect the intermediate classes (bare ice and thin ice) to be somewhat overestimated.

3.2 Optical measurements

The reflected radiance from the Spectralon reference plate was collected twice (before and after the flights), and only the reflected surface radiance were collected during the flights. The radiance reflected from the surface is affected by the amount of clouds, and may change as clouds drift, so variable light conditions will result in an error in the spectral RF (both in the spectral signature and the absolute value). To reduce the effect of changing light conditions and overcome some of the shortcomings with the set-up, the spectral RF measurements were normalized with the ratio of the reflectance over a large, homogeneous, snow-covered surface both from inside the helicopter when flying and from the ground afterwards. This approach was also used in Allison et al. (1993) on their optical airborne measurements.

3.3 Data fusion

The reflectance measurements and images were co-located based on time and position. For each reflectance spectrum the footprint in the image was identified and the fractions of sea-ice types within that footprint calculated (Fig. 5). As the co-location was based on time (resolution 1 s) and the helicopter had a typical speed of 25-30 ms^{-1}, some error in the co-location procedure must be assumed. Angle and tilt of the helicopter change the direction of the spectrometer footprint, and measured reflectances are subject to errors if the surface is tilted. The effect is largest under clear sky, but also evident for overcast conditions (Allison et al., 1993). No attempt was made to correct for this.

[Fig. 5 about here.]

3.3.1 Spectral unmixing

Spectral unmixing is an unsupervised classification technique based on the spectral reflectances, which models the measured reflectance spectra as a linear combination of characteristic reference spectra (so-called endmembers). If the endmembers are known, the product of the spectral unmixing gives the fraction of each sea-ice type within the spectrometer footprint by solving

Eq. (1) in a least square manner (Vikhamar, 2003).

$$\mathbf{f} \cdot \alpha_{\mathbf{ch}}(\lambda) = \mathbf{r}(\lambda) \tag{1}$$

$\mathbf{f}$ is the $(m \times 4)$ matrix of fractions for the four sea-ice types for m images, $\mathbf{r}(\lambda)$ is the $(m \times n)$ matrix of measured reflectance spectra for n wavelength bands, and $\alpha_{\mathbf{ch}}(\lambda)$ is the $(4 \times n)$ characteristic albedo curves for each sea-ice type. The endmembers were identified directly from the classified images (the fraction of sea-ice types within the spectrometer footprint in the image) and the spectral reflectance measurements by using inverse spectral unmixing. This was done in a partly iterative manner, by first assuming standard characteristic albedo curves from previous measurements, following Tschudi et al. (2001). Based on the classified image fractions and the endmembers, an additional measure of spectral RF was calculated by weighting the characteristic spectra with the fractions in the spectrometer footprint, following the method of Perovich et al. (2002).

4 Results and discussion

On 3rd June the most consistent dataset of the expedition was obtained under mostly overcast conditions, and these data are further investigated in this section. The temperature on 3rd June was above 0°C and the snow surface was wet. However no melt ponds were visible (neither from ground nor air). Altogether 592 images, 1487 spectra and 26488 thickness signals were collected, standardized and classified (Sec. 3). The airborne measurements were collected from a transect going west-north-east for the optical flight and west-east for EM-measurements (Fig. 1b). The two west transects, seen relative to the ice surface, become more separated to the west as the ice in the western Fram Strait drifts relatively fast in a S-SW direction. From 3°W to 4° 36' W the flight-line for the EM measurements coincides more or less with the first east-west transect of the optical flight, so these sections were selected for comparing sea-ice thicknesses with findings and characteristics from the optics and photography analysis. Taking the relatively fast ice drift in the western Fram Strait into account, this comparison is only possible when assessing the general ice regime characteristics, and not individual floes.

4.1 Sea-ice types

The test and training data sets (Sec. 3.1.3) were created by manually classifying 120 000 pixels within 23 images to each of the four sea-ice types. The best set of features were selected according to Fisher Discriminant Analysis (Sec. 3.1.2) by performing 50 Monte Carlo simulations where the test and training set were chosen randomly within the set of classified pixels for each simulation. The best features for separating between the sea-ice classes were found to be the three RGB intensities, the coefficient of variance (standard deviation divided by the mean), the entropy (measure of histogram uniformity) and the GLCM homogeneity. A range of one standard deviation around the mean for the RGB intensities was found to separate the four classes completely, only with slight overlap between thin ice and open water. The co-efficient of variance was high for thin ice, and the mean +/- one standard deviation separated it from the other classes, while the mean of the entropy +/- one standard deviation separated thick bare ice from thin ice. No such simple relationship was found for the GLCM homogeneity.

The neural network proved to be extremely efficient for discriminating between the four sea-ice types, with only 1.06% classification error on the test set. The confusion matrix gives the number of times a feature vector belonging to class i (row) is classified to class j (column), where i, j are the four classes (Table 4). The correct classified pixels are along the diagonal from upper left to lower right. The test resulted in 98-100% correct classification for the different classes, which is more than sufficient for routine use. Open water was easily distinguished from the other types, with only 0.2% confusion with thin ice. Thick bare ice was most often confused with snow-covered ice (1.0%). Large scale structures such as large areas of open water or snow-covered sea ice were generally easily identified (Fig. 5). At smaller scales, the classifier was less accurate due to down-scaling and smoothing when calculating the texture features. Errors at the edges between classes are typical as the median filter (Sec. 3.1.3) does not completely remove this. The consequence is that the intermediate sea-ice types (thick bare ice and thin ice) were over-estimated. Also, the test set results under-estimate the classification error since the pixels in the test set were chosen within larger, relative homogeneous areas of the individual sea-ice types, and very few pixels were on the edge between classes. For images outside the test set, larger classification error is expected, particularly for thick bare ice and thin ice covering relative small areas. Since the textural features are averages over a 3.5x3.5 m (7x7 pixels) window, features smaller than this, *e.g.* wind shaped formations in snow, small ice floes and blocks, pancake ice *etc.* will be removed by smoothing and are not identified. This is partly why the thin ice class (with mixed brash ice) was introduced.

[Table 4 about here.]

The fractional area of snow-covered ice, thick bare ice, thin ice and open water as a function of longitude bands show considerable spatial variability, with snow-covered ice fractions varying from 0 to 100%, but with an average high ice concentration over the entire profile (Figs. 1b and 6a). The two ice classes without snow cover represent only a small portion compared to snow-covered ice and open water. In the west there are more areas of open water compared to the east. Overall, the average ice concentration (total of snow covered, thick and thin ice) was 90.4%, with average fractions for snow-covered sea ice of 81.0%, thick bare ice 4.0%, thin ice 5.3% and open water 9.6%. For comparison, the average sea-ice concentration compiled from The Ocean and Sea Ice Satellite Application Facility (OSI-SAF-http://www.osi-saf.org, derived from special sensor microwave/imager data SSM/I) were 82.8% (with median 83.7% and range 64.0-93.9%) for the twelve 10 km resolution pixels inside the rectangular area of Fig. 1a.

[Fig. 6 about here.]

The sea-ice types were also calculated from the optical measurements by means of spectral unmixing. Compared to the neural network classification of the digital images (taken to represent the "true classes"), this resulted in an over-estimation of open water fractions to the west and thick bare ice fractions to the east (Fig. 6). The spectral unmixing technique was not very appropriate for detecting thin ice as the thin ice fraction in the west is detected as open water in Fig. 6, due to large scatter in the spectra used for determining the endmembers. The correlation coefficient between the fractions from the neural network and spectral unmixing was highest for snow-covered ice (0.90) and open water (0.81), whereas it was substantially smaller for the two intermediate sea-ice classes (0.51 for thick bare ice and 0.58 for thin ice). Limitations in the co-location is probably responsible for some of the deviations, as the intermediate types cover smaller spatial areas, and thereby are more sensitive to small off-sets. A scatter-plot of neural network fractions (f_{NN}) against spectral unmixing fractions (f_{SU}) for the four sea-ice classes (Fig. 7), show a cluster along $f_{NN} = 1$ (Fig. 7a), meaning that the spectral unmixing under-estimates the snow-covered ice. For thick bare ice and open water (Figs. 7b and d, respectively) the trend is opposite, with clusters along $f_{NN} = 0$, implying that the spectral unmixing over-estimates those fractions. For thin ice (Fig. 7c) the congestion is along $f_{SU} = 0$, meaning that the spectral unmixing has problems in detecting thin ice, as discussed above. The overall root mean square error for using spectral unmixing to estimate the fractions are 0.034, 0.027, 0.021 and 0.028 for snow-covered ice, thick bare ice, thin ice and open water, respectively.

[Fig. 7 about here.]

The EM thickness measurements can also be used to determine the sea-ice types by separating open water (thickness below 0.05 m), thin ice (thickness between 0.05-0.3 m) and thick snow-covered ice (thickness above 0.3 m). It is not possible to partition the snow and the ice from the EM measurements, since the snow thickness is always included in the total thickness. The fractions from the EM measurements show different characteristics, with no trend, and mostly thick snow-covered sea ice at all longitudes (Fig. 6d). These fractions can not be compared directly with the others, as the two flight lines were not concurrent and the ice drifted fast, so the comparison is more a statistical than a point-to-point comparison. By totaling the snow covered and thick ice fractions from the neural network and comparing it with the thick ice fraction from the EM measurements, the correlation coefficient is as low as 0.25, with corresponding correlation coefficients between the thin ice and open water fractions of 0.34 and 0.08, indication low and no correlation, respectively.

4.2 Reflectance

For the calculation of the spectral reflectance factor measurements, only the first east-west transect of the optical flight was used, as the light conditions changed too much over time to include all measurements. The broadband RF, calculated from the spectral RF by weighing the spectral RF with an appropriate solar irradiance spectrum for cloudy conditions (Grenfell and Perovich, 2004), is hereinafter called the measured broadband RF. It shows a relative high mean broadband RF over the entire transect, however higher in the east than in the west (Fig. 8a). Broadband albedos are higher for cloudy sky than clear sky (Brandt et al., 2005), so this may indicate more clouds in the east. The average measured broadband RF was 0.73 with standard deviation of 0.33. The broadband RF was also calculated from the inverse spectral unmixing (hereinafter called calculated broadband RF), which corresponds well with the measured broadband RF (Fig. 8a). The calculated broadband RF does not increase towards the east since it has its upper threshold value set at 0.8711 corresponding to the broadband RF of a snow-covered sea ice endmember. The scatter plot of measured versus calculated broadband RF (Fig. 8b) show that the measurements coincide around the 1:1 line, with a correlation coefficient of 0.94. Measured broadband RF are higher than calculated broadband RF for high values (the measured broadband RF frequently exceeds one), with a weak tendency of the opposite for small broadband RF values. If the measured broadband RF is taken to represent the ground truth reflectance factor, the overall root mean square error for the calculated broadband RF is 0.048.

[Fig. 8 about here.]

The endmembers for the four sea-ice types were calculated from inverse spectral unmixing, and have spectral signatures similar to other albedo measurements (Brandt et al., 2005; Grenfell and Perovich, 2004; Gerland et al., 2004). However, the set-up affected the endmembers by giving more noisy (jagged) spectras with an unexpected dip at UV wavelengths and substantial noise at high wavelength. The endmember curves were averaged with a running mean (over 30 nm) to achieve smoother and more realistic curves (Fig. 5). In addition the measured broadband RF were normalized to have the same mean as the calculated broadband RF.

The mean and standard deviations of the broadband RF were calculated for each sea-ice type by including only the spectra for those spectrometer footprints having a fraction larger than 90% of one sea-ice type (Table 5), *i.e.* not more than 10% of the pixels within the spectrometer footprint may belong to other classes. For bare thick ice, no spectrometer footprint had a fraction of 90% or more, so the threshold limit was reduced to 75%, and therefore the error in the mean broadband RF for thick bare ice may be high (despite a low standard deviation in Table 5). Overall, the broadband RF corresponds well with values found in the literature for broadband albedo. The broadband RF for open water was slightly higher than corresponding albedo values from Brandt et al. (2005), because the open water was mixed with the other sea-ice types, all having higher broadband RF. Allison et al. (1993) also determined higher open water albedos than usual, due to snow-covered ice in the vicinity of the open water scene. The broadband RF of thin ice was 0.23, corresponding to values of young grey ice (Brandt et al., 2005), but with extremely large standard deviations due to the thin ice broadband RF ranging from snow-covered ice to open water in its footprints. Previous measurements show that for bare ice, the reflectance factor has a lower value than the albedo (Perovich, 1994). However, the thick ice broadband RF was higher than what is reported for the snow-free first year ice albedo (Brandt et al., 2005). This is probably due to mixing with snow-covered ice (on average 15% of the area within the footprint was snow covered). The nadir reflectance factor and albedo should be similar at all wavelengths for snow (Perovich, 1994), and this is in fact shown here where the snow-covered sea ice has a broadband RF well inside the range of expected albedo values for snow (Paterson, 2001), and slightly higher than others (Brandt et al., 2005; Grenfell and Perovich, 1984).

[Table 5 about here.]

4.3 Sea-ice thickness

From the total set of ice thickness data obtained, the thickness distribution at about 79° N exhibits a clear regional gradient from 10°W to 2°W; from thicker ice with a broad thickness distribution in the west to thinner ice with a more narrow thickness distribution in the east (Gerland et al., 2006). The modal ice thickness increases from east to west from about 2 m to almost 3 m (Fig. 9c). Most of the ocean along the flight line is covered with ice, but leads occur regularly. However, the amount of open water of narrow cracks and leads can be under-estimated with the EM technique due to the large footprint.

Few ridges thicker than 6 m were observed. In general, the thickest ridges were found in the western part of the transect, with one ridge reaching a thickness of more than 10 m. However, airborne EM derived thicknesses can under-estimate thicknesses of ridges by a factor 2 or more (?), indicating that real maximum ridge thickness might be at 20 m or more. The probability density functions illustrate that the ice is different in the west and east of the investigation area (Fig. 10), which is consistent with the regional trend beyond the section selected for this paper (Gerland et al., 2006). For both areas the density functions have two main modes, the first one is around zero for open water (with uncertainties) and the second one thicker, consisting of multiyear and ridged first-year, ice. At the marginal ice zone in the east, the modal ice thickness is 1.8 m (Fig. 10a). Further west the distribution indicates thicker ice with the main mode at 2.6 m and an additional prominent first-year ice mode at 1.1 m (Fig. 10b). The average sea-ice thickness including snow was 2.1 m with a standard deviation of 1.3 m.

[Fig. 9 about here.]

[Fig. 10 about here.]

4.4 Data fusion

The combination of measurements from each instrument clearly shows that variations in measured broadband RF coincide well with changing sea-ice types (Fig. 9), where high broadband RF corresponds to large fractions of snow-covered ice and low broadband RF corresponds to large fractions of open water. Small fractions of the two intermediate ice types, *e.g.* at 3.7° W, lead to a visible reduction in the broadband RF. The correlation coefficient between measured broadband RF and fractional coverage from the digital images was 0.72 for snow-covered ice (Fig. 11a) and -0.61 for open water (Fig. 11b), with large scatter of the samples. The correlation coefficient is negative because a higher fraction of open water leads to a reduced broadband RF. The measured broadband RF is not very dependent on the fractional coverage of thick ice nor thin ice (correlation coefficients of -0.16 and -0.30, respectively). Also these correlations were negative as an increased fraction results in reduced broadband RF (compared against that of snow-covered ice, which was dominant). The correlations were relatively low because the intermediate sea-ice types covered smaller areas and are more vulnerable against small offsets in the footprint of the camera and spectrometer.

[Fig. 11 about here.]

The correlation between the sea-ice concentration and measured broadband RF was 0.69. This was higher than the correlations found by Laine (2004) using remote sensing data in the Arctic Ocean and Northern Hemisphere (0.34 and 0.56, respectively).

5 Conclusions

In this paper a dataset that provides information that can be employed to obtain a description of the sea ice regime has been presented. The dataset provides information on the sea-ice type, albedo and total ice thickness observed along a transect. More importantly, the methods presented allow the different components of the dataset to be collected and compared in a consistent manner to obtain the maximum amount of information. The principal information from the three methods described gave sea-ice types from digital photography, the spectral and broadband reflectance factor from the spectrometer and the total sea-ice thickness from the airborne electromagnetic bird. Together these three datasets provide a comprehensive description of the complex sea ice environment: the sea-ice concentration, described by combining the sea-ice types and separating it from open water; sea-ice volume, the extent multiplied with the thickness; and the energy balance determined from the optical measurements. If one component of the data set is missing, then important information may be lost. For example, the east-west ice thickness gradient does not appear in the sea-ice types or optical observations. Since most of the sea ice is covered by relatively thick snow, and the albedo is completely determined by a snow cover of only a few cm thickness (Allison et al., 1993), snow-covered multiyear ice and first year ice are difficult, if not impossible, to distinguish without thickness measurements. However, if one component is missing (due to the lack or failure of instruments) then the necessary information can, to some extent, be extracted from the other measurements, albeit with increased error. The average root mean square errors for employing spectral unmixing for sea ice classification are 0.034, 0.027, 0.021 and 0.028 for snow-covered ice, thick bare ice, thin ice and open water, respectively, and for employing inverse spectral unmixing for broadband RF is 0.048. The same does not apply for the EM measurements. Although the fractional coverage of sea-ice types can be extracted from all three components individually, the neural network uses textural features for classifying the digital images, spectral unmixing uses the optical characteristics for classifying the reflectance measurements, and the thresholding technique uses the total sea-ice thickness for classifying the EM-measurements, hence the fractions will be biased depending on the property used.

The average sea-ice fractions for the over flown area were 81.0% for snow-covered ice, 4.0% for thick bare ice, 5.3% for thin ice and 9.6% for open water, thus the average sea-ice concentration was 90.3%. The provided techniques are quite general so only minor changes are required to include for example melt ponds or other necessary sea-ice types if the transects are conducted during summer time. The average measured broadband RF was 0.73 with standard deviation 0.33, and the average total sea-ice thickness (including snow) was 2.1 m with standard deviation 1.3 m. The average sea-ice volume is thus 2.1 times the area. Further, relative high correlations were found between the measured albedo and sea-ice concentration (0.69).

This initial study sheds light on the enormous potential of integrated airborne surveys over sea ice with modern methods. Improvements of the individual set-ups and steps will reduce the temporal and spatial bias. This particularly concerns the optical measurements. Future solutions will include optimizing systems so that all measurements can be performed from the same flight. The optical sensors will be mounted outside the helicopter to avoid effects from windows, and the problem introduced by varying incoming solar radiation will be addressed by direct measurements of the incoming radiation, parallel to the nadir reflectance measurements. Other improvements include: co-location procedure, storage of raw images and the installation of a tilt-meter to correct for the angle and tilt of the helicopter. Some of these improvements are already under development and will be applied during campaigns as a part of projects in the International Polar Year 2007-2009. With such an improved set-up, large amounts of sea ice measurements processed with the described methodology will be an extremely valuable dataset for the validation of general circulation models and remote sensing products. In addition, for applications with unmanned aerial vehicles such an integrated airborne approach is required.

6 Acknowledgments

We thank the captain and crew on board Coastguard K/V Svalbard during the expedition to the Fram Strait spring 2005, and also Terje Gundersen and Håvard Dahle from Airlift. Norwegian Polar Institute and Department of Environment is acknowledged for financing the cruise. We would like to thank O. Pavlova for providing the sea-ice concentrations from The Ocean and Sea Ice Satellite Application Facility (Fig. 1a) and O.-M. Olsen for the helicopter tracks on the SAR image (Fig. 1b). Fred Godtliebsen and Jan-Gunnar Winther are acknowledged for comments during an early stage of the work. We also thank the reviewer for his many comments, substantially improving this paper. C. A. Pedersen received funding from the Research Council of Norway.

References

Allison, I., Brandt, R., and Warren, S. (1993). East Antarctic Sea Ice: Albedo, Thickness Distribution, and Snow Cover. *Journal of Geophysical Research*, 98:12417–12429.

Andersen, S., Breivik, L.-A., Eastwood, S., Godøy, Ø., Lind, M., Porcires, M. and Schyberg, H. (2005). *Sea Ice Product Manual*. Norwegian and Danish Meteorological Institutes.

Armstrong, T., Roberts, B., and Swithinbank, C. (1966). *Illustrated Glossary of Snow and Ice*. Special publication number 4. Scott Polar Research Institute, Cambridge.

Barber, D. G. and Le Drew, E. F. (1991). SAR Sea Ice Discrimination Using Texture Statistics: A Multivariate Approach. *Photogrammetric Engineering & Remote Sensing*, 57(4):385–395.

Bogdanov, A. V., Sandven, S., Johannessen, O. M., Alexandrov, V. Y., and Bobylev, L. P. (2005). Multisensor Approach to Automated Classification of Sea Ice Image Data. *IEEE Transactions on Geoscience and Remote Sensing*, 43(7):1648–1664.

Brandt, R. E., Warren, S. G., Worby, A. P., and Grenfell, T. C. (2005). Surface Albedo of the Antarctic Sea Ice Zone. *Journal of Climate*, 18:3606–3622.

Derksen, C., Piwowar, J. and LeDrew, E. (1997). Sea-Ice Melt-Pond Fraction as Determined from Low Level Aerial Photographs. *Arctic and Alpine Research*, 29(3),345–351.

Fetterer, F. and Untersteiner, N. (1998). Observations of Melt Ponds on Arctic Sea Ice. *Journal of Geophysical Research*, 103(C11):24821–24835.

Gerland, S., Haas, C., Hall, R., Holfort, J., Hansen, E., Løyning, T., and Renner, A. (2006). Spring Sea Ice Thickness in the Western Fram Strait: Preliminary Results. In Wadhams, P. and Amanatidis, G., editors, *Arctic Sea Ice Thickness: past, present & future. Proceedings of an international workshop at Rungstedgaard, Denmark, November 2005*, Climate Change and Natural Hazard Series 10. European Commission EUR 22416.

Gerland, S., Haas, C., Nicolaus, M., and Winther, J.-G. (2004). Seasonal Development of structure and Optical Properties of Fast Ice in Kongsfjorden, Svalbard. In Wiencke, C., editor, *The Coastal Ecosystems of Kongsfjorden, Svalbard*, number 492, pages 26–34. Alfred Wegner Institute for Polar & Marine Research.

Gonzalez, R. C. and Woods, R. E. (1992). *Digital Image Processing*. Addison-Wesley Publishing Company.

Grenfell, T. and Perovich, D. K. (2004). Seasonal and Spatial Evolution of Albedo in a Snow-Ice-Land-Ocean Environment. *Journal of Geophysical Research*, 109:1–15.

Grenfell, T. C. and Perovich, D. K. (1984). Spectral Albedos of Sea Ice and Incident Solar Irradiance in the Southern Beaufort Sea. *Journal of Geophysical Research*, 89(C3):3573–3580.

Haas, C., Lobach, J., Hendricks, S., Rabenstein, L. and Pfaffling, A. (2008).

Helicopter-Borne Measurements of Sea Ice Thickness, Using a Small and Lightweight, Digital EM System. *Journal of Applied Geophysics*, in press.

Haas, C., Gerland, S., Eicken, H., and Miller, H. (1997). Comparison of Sea-Ice Thickness Measurements Under Summer and Winter Conditions in the Arctic Using a Small Electromagnetic Induction Device. *Geophysics*, 62(3):749–757.

Haykin, S. (1999). *Neural Networks - A Comprehensive Foundation*. Prentice Hall.

Johnson, R. A. and Wichern, D. W. (2002). *Applied Multivariate Statistical Analysis*. Prentice Hall.

Kwok, R., Cunningham, G. F., and Pang, S. S. (2004). Fram Strait Sea Ice Outflow. *Journal of Geophysical Research*, 109(C01009).

Laine, V. (2004). Arctic Sea Ice Regional Albedo Variability and Trends, 1982-1998. *Journal of Geophysical Research*, 109(C06027).

Lythe, M., Hauser, A., and Wendler, G. (1999). Classification of Sea Ice Types in the Ross Sea, Antarctica from SAR and AVHRR Imagery. *International Journal of Remote Sensing*, 20(15 & 16):3073–3085.

Markus, T., Cavalieri, D. J., and Ivanoff, A. (2002). The Potential of Using Landsat 7 ETM+ for the Classification of Sea-Ice Surface Conditions during Summer. *Annals of Glaciology*, 34:415–419.

Massom, R. and Comiso, J. C. (1994). The Classification of Arctic Sea Ice Types and the Determination of Surface Temperature Using Advanced Very High Resolution Radiometer Data. *Journal of Geophysical Research*, 99(C3):5201–5218.

Nicodemus, F. E., Richmond, J. C., Ginsberg, I. W., and Limperis, T. (1977). Geometrical Considerations and Nomenclature for Reflectance. Technical report, U.S. Department of Commerce, National Bureau of Standards.

Paterson, W. S. B. (2001). *The Physics of Glaciers*. Butterworth Heinemann, Third edition.

Perovich, D. K. (1994). Light Reflection from Sea Ice During the Onset of Melt. *Journal of Geophysical Research*, 99(C2):3351–3359.

Perovich, D. K., Tucker, W. B. III and Ligett, K. A. (2002). Aerial Observations of the Evolution of Ice Surface Conditions during Summer. *Journal of Geophysical Research*, 107(C10):8048–8062.

Perovich, D. K., Light, B., Eicken, H., Jones, K. F., Runciman, K. and Nghiem, S. V. (2007). Increasing Solar Heating of the Arctic Ocean and Adjacent Seas, 1979-2005: Attribution and Role in the Ice-Albedo Feedback. *Geophysical Research Letter*, 34(L19505).

Pfaffling, A., Haas, C., and Reid, J. (2007). A Direct Helicopter EM Sea Ice Thickness Inversion, Assessed with Synthetic and Field Data. *Geophysics*, 72:F127-F137.

Secretary of World Meteorological Organization (1970). WMO Sea-Ice Nomenclature. Technical report, World Meteorological Organization.

Steffen, K. (1986). Atlas of the Sea Ice types - Deformation Processes and Openings in the Cce. Technical report, ETH Geographisches Institut.

Theodoridis, S. and Koutroumbas, K. (1999). *Pattern Recognition*. Academic Press.

Tschudi, M. A., Curry, J. A., and Maslanik, J. A. (2001). Airborne Observations of Summertime Surface Features and Their Effect on Surface Albedo during FIRE/SHEBA. *Journal of Geophysical Research*, 106(D14):15335–15344.

Vikhamar, D. (2003). *Snow-Cover mapping in Forests by Optical Remote Sensing*. PhD thesis, Faculty of Mathematics and Natural Science, University of Oslo, Norway.

Vinje, T. (2001). Fram Strait Ice Fluxes and Atmospheric Circulation: 1950-2000. *Journal of Climate*, 14(16):3508–3517.

List of Figures

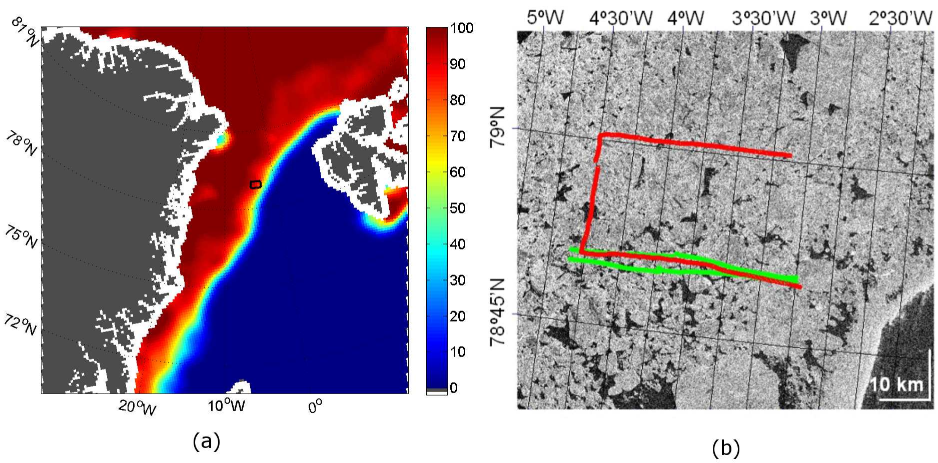

Fig. 1. (a) Sea-ice concentration (in percent) in the Fram Strait on 3rd June 2005 from passive microwave data with 10 km resolution from The Ocean and Sea Ice Satellite Application Facility (OSI-SAF-http://www.osi-saf.org), with Svalbard to the east and Greenland to the west (grey is land area and white is no data). The rectangle marks the investigated area 78.00°-79.05° N and 2.8°-4.8° W. (b) Flight track for the two helicopter flights on 3rd June 2005 in the Fram Strait. The red track is for the optical and photography measurements, while the green is for the electromagnetic measurements. The SAR image is from 07.31 GMT, the optical flight was compiled between 07:27-08:19 GMT, and the electromagnetic flight between 11:08-12:32 GMT. The sea ice in the Fram Strait drifts relative fast in S-SW direction. Therefore, while the two tracks coincide in position, they did not cover the same area relative to the ice.

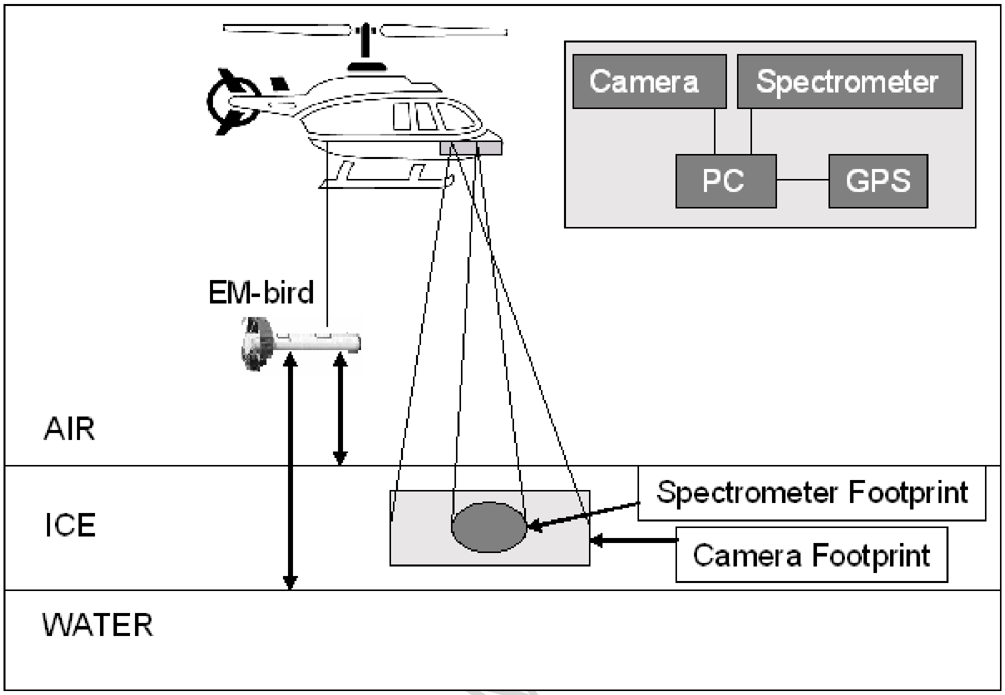

Fig. 2. Set up for the two different helicopter flights. One being the optical flight with digital camera and spectrometer fore-optics mounted on the floor of the helicopter. The cameras and spectrometers field-of-view are shown relative to each other. The other being the electromagnetic (EM) flight, using an EM-bird with transmitter and receiver coils and a laser altimeter. The ice thickness is obtained from the difference of the bird's height above the water and ice surface.

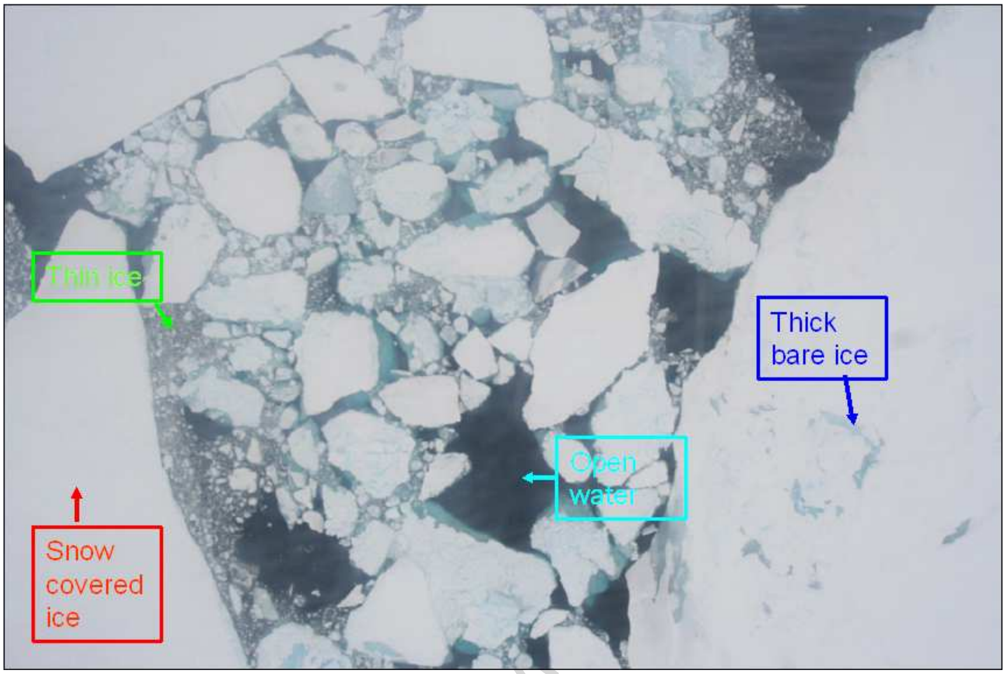

Fig. 3. Sea ice image example where each of the four sea-ice types are represented. The colors correspond to the spectra in Fig. 5.

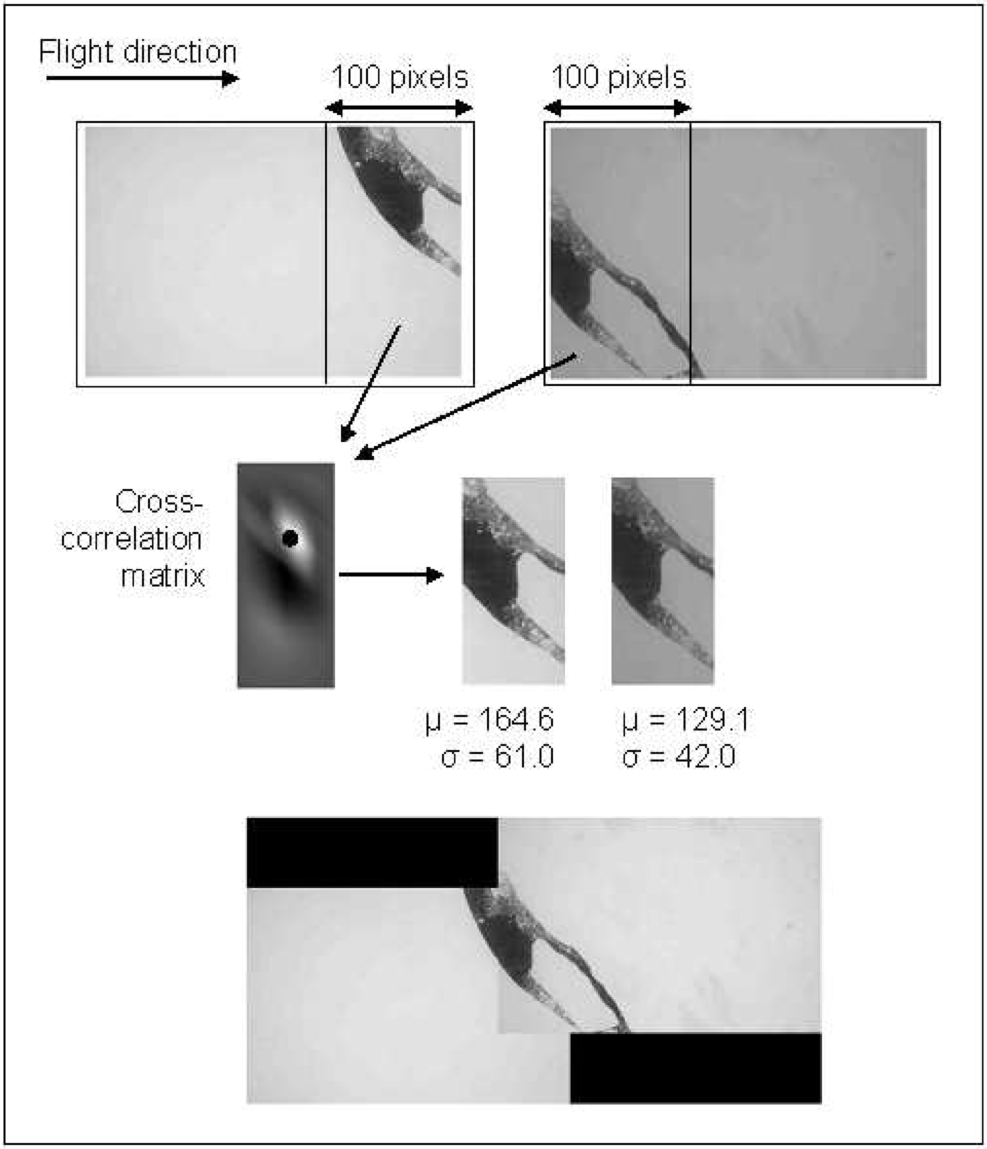

Fig. 4. The standardizing procedure for getting a homogeneous time series of the airborne images. The upper panels show two overlapping images with different brightness and contrast. The two sub-images (of 100 pixels width, marked with a frame) were cross-correlated, giving the matrix in the middle left. The black dot marks the maximum in the cross-correlation matrix, giving the best alignment between the two sub-images (shown in the middle-right). The second sub-image was scaled to have the same mean (μ) and standard deviation (σ) as the first. The bottom image shows the two overlapping images after the standardization procedure.

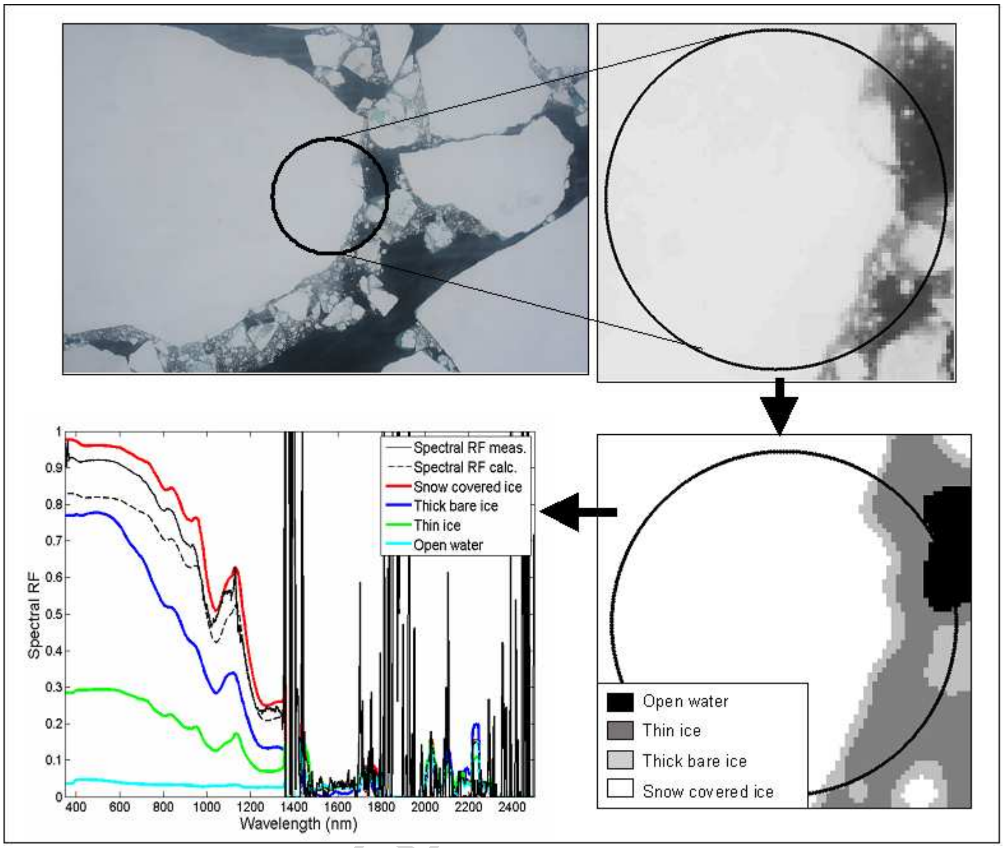

Fig. 5. An example of the co-location procedure of the data, with the original RGB image (upper panel, left), and the footprint of the spectrometer co-located within the grey-leveled, down-sampled image (upper panel, right). The classified subset of the image (bottom panel, right) gives a fraction of 75.8%, 5.5%, 16.0% and 2.7% for snow-covered ice, thick bare ice, thin ice and open water, respectively, with the corresponding characteristic curves (endmembers) for the four sea-ice types (in color) together with the measured and calculated spectral reflectance factor (RF) (bottom panel, left).

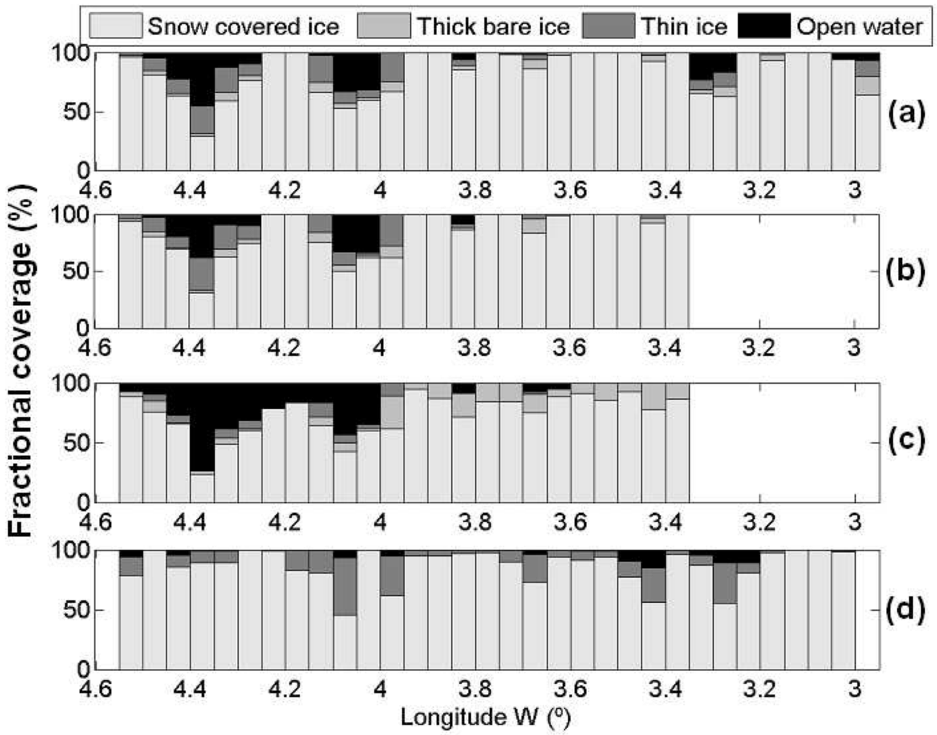

Fig. 6. Fractional coverage of open water, thin ice, bare thick ice and snow-covered ice as a function of longitude bands of 0.05°. (a) neural network classification from photography, (b) neural network classification from photography within the foot-print of the spectrometer (only a subset of the image is used), (c) spectral unmixing from optical measurements, (d) classification based on EM thickness measurements. The bottom panel only has three classes (open water (black), thin ice (grey) and thick, snow-covered ice (light grey)).

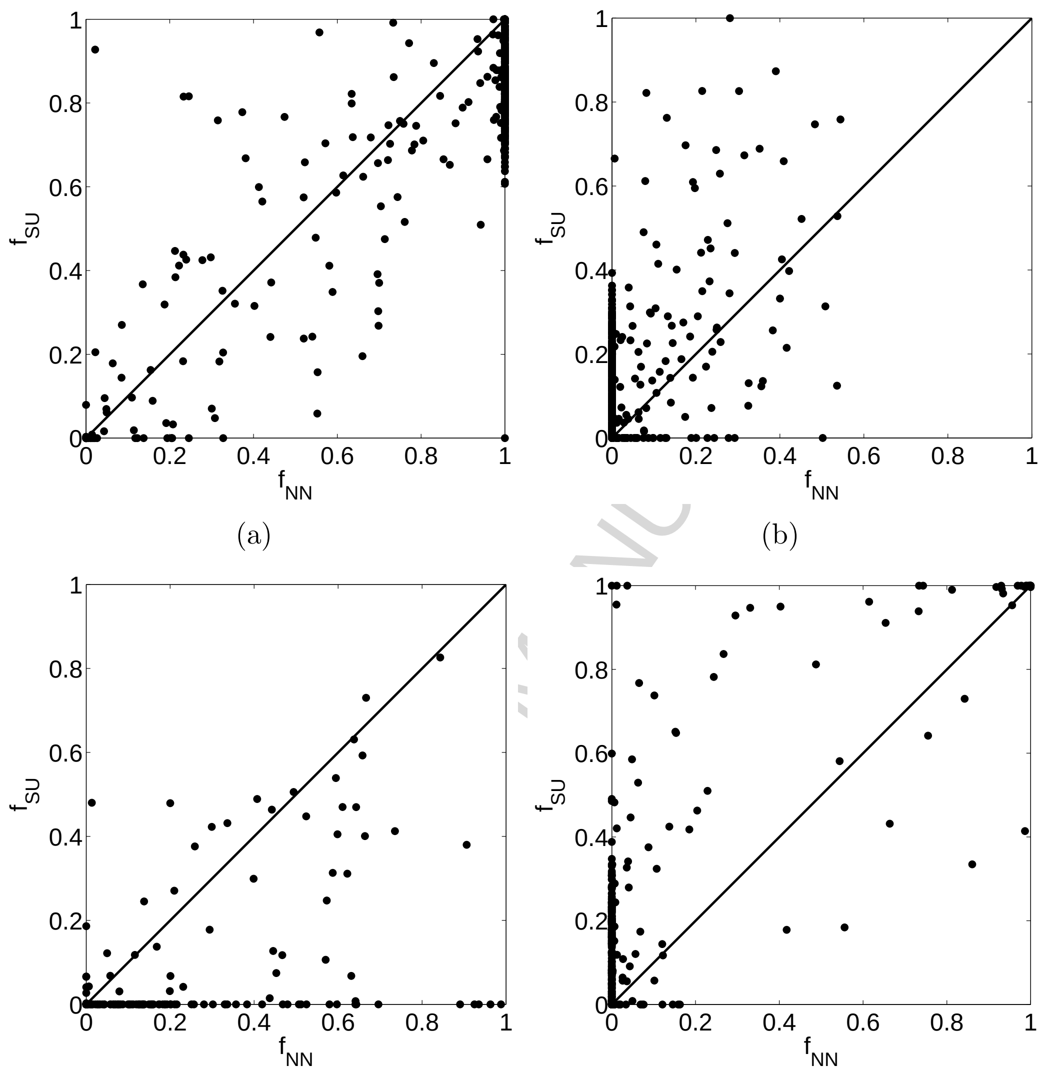

(a)

(b)

(c)

(d)

Fig. 7. Scatter plot between sea-ice fractions as calculated from neural network (f_{NN}) and spectral unmixing (f_{SU}). The 1:1 line indicates linear correlation. (a) is for snow-covered ice ($\rho = 0.90$), (b) thick bare ice ($\rho = 0.51$), (c) thin ice ($\rho = 0.58$) and (d) open water ($\rho = 0.91$), where ρ is the correlation coefficient.

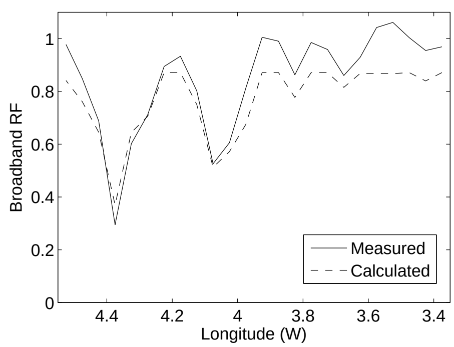

(a)

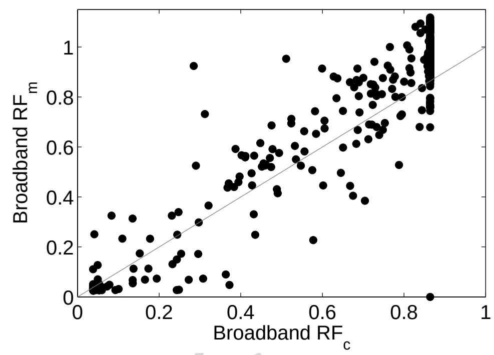

(b)

Fig. 8. (a) Measured and calculated broadband reflectance factor (broadband $\mathrm{RF_m}$ and broadband $\mathrm{RF_c}$, respectively) as a function of longitude bands of 0.05°. (b) Scatter plot of measured broadband $\mathrm{RF_m}$ against calculated broadband $\mathrm{RF_c}$. The correlation coefficient is 0.94.

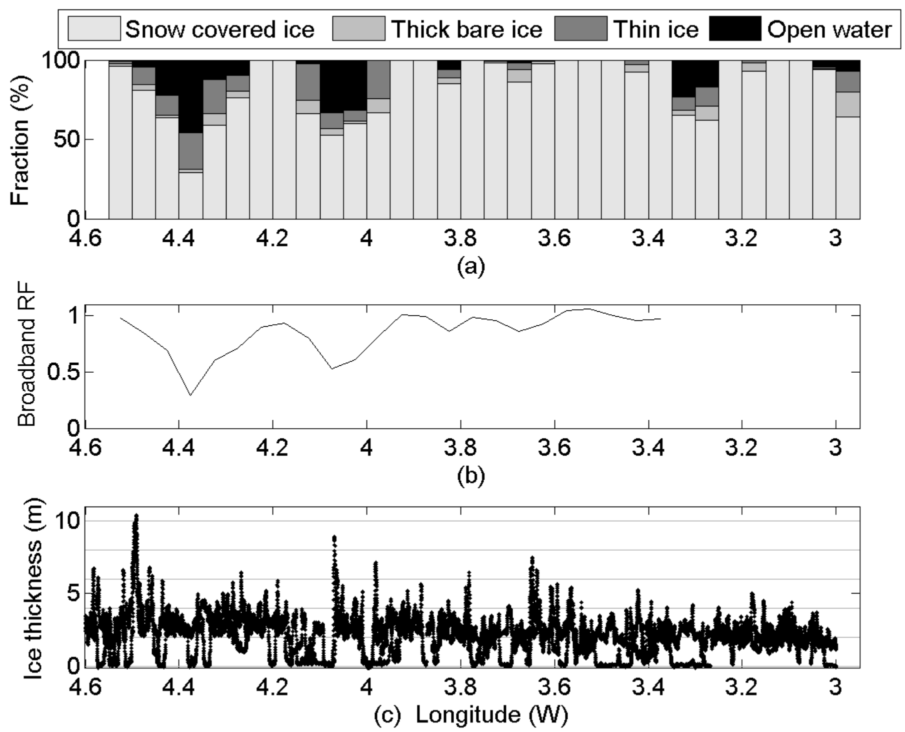

Fig. 9. (a) Average fractional coverage of the individual sea-ice types from the classified photographies and (b) average measured broadband reflectance factor (RF) as a function of longitude for 0.05° longitude bands. (c) Total sea-ice thickness (ice plus snow) as measured from the electromagnetic bird.

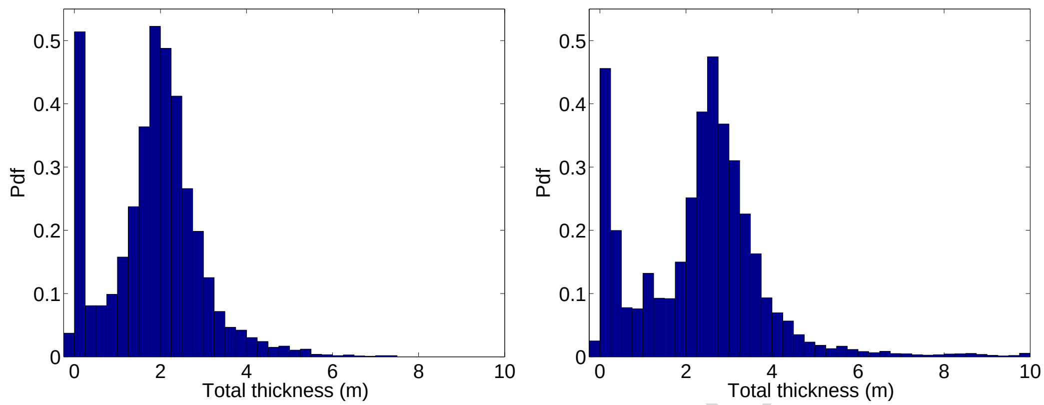

(a) (b)

Fig. 10. Probability density function (Pdf) of the total sea-ice thickness (sea ice plus snow) from the two transects 3.0-3.8° W in (a) and 3.8-4.6° W in (b) from the electromagnetic bird.

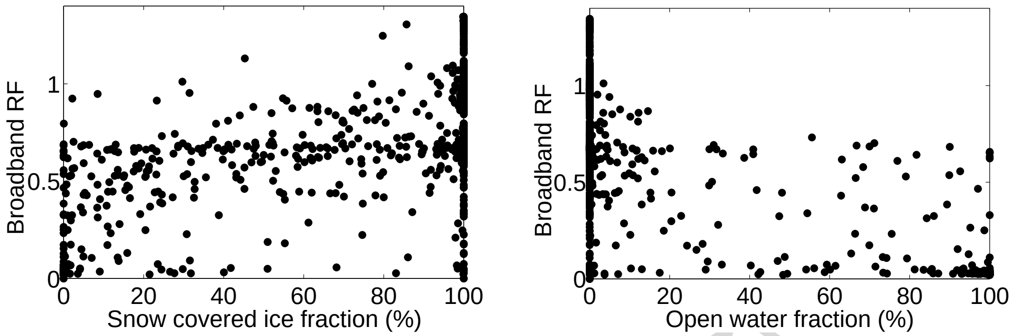

(a) (b)

Fig. 11. Scatter-plots of measured broadband reflectance factor (broadband RF) and fractional snow-covered ice in (a) and fractional open water in (b), with correlation coefficients of 0.72 and -0.61, respectively.

List of Tables

Information	Instrument	Sampling frequency
Fractional sea-ice types	Canon EOS 350D digital camera	5 s
Reflectance	ADS FieldSpec Pro spectrometer	2 s
Ice thickness	Electromagnetic bird	0.1 s

Table 1
Airborne measurements

Class index	Description of sea-ice types
I	Snow-covered sea ice
II	Thick bare sea ice
III	Thin ice (combined brash ice)
IV	Open water

Table 2
Observed sea-ice types in the Fram Strait in spring 2005 before the onset of summer melt.

	Features
1	Red intensity
2	Green intensity
3	Blue intensity
4	Grey-level intensity
5	Mean intensity
6	Variance
7	Skewness
8	Kurtosis
9	Entropy
10	Energy
11	Coefficient of variance
12	GLCM contrast
13	GLCM energy
14	GLCM homogeneity

Table 3
Textural features for sea ice classification. Features 5-11 are based on first order statistics, while features 12-14 are from second-order statistics and the grey-level-co-occurrence matrix (GLCM) (Theodoridis and Koutroumbas, 1999)).

	Snow-covered ice	Thick bare ice	Thin Ice	Open water
Snow-covered ice	**98.4**	1.3	0.2	0.1
Thick bare ice	1.0	**98.3**	0.5	0.2
Thin Ice	0	0.6	**99.2**	0.2
Open water	0	0	0.2	**99.8**

Table 4
The confusion matrix for neural network classification on the test set, when the best feature combination (the three RGB intensities, coefficient of variance, entropy and GLCM homogeneity) was used. The confusion matrix gives the number of times a feature vector belonging to class i (along the rows) is classified to class j (along the columns). The correct classified pixels are in bold along the diagonal.

	Snow-covered ice	Thick bare ice	Thin ice	Open water
Mean(broadband RF)	0.86	0.63	0.23	0.09
σ(broadband RF)	0.22	0.16	0.36	0.16
$\sharp$ of samples	1058	7	7	99

Table 5
The mean and standard deviation (σ) of broadband reflectance factor (broadband RF). The bottom row gives the number of samples used for the calculations.